Hepatic Lesions: Improved Image Quality and Detection with the Periodically Rotated Overlapping Parallel Lines with Enhanced Reconstruction Technique—Evaluation of SPIO-enhanced T2-weighted MR Images[1]

Yuusuke Hirokawa, MD
Hiroyoshi Isoda, MD, PhD
Yoji S. Maetani, MD, PhD
Shigeki Arizono, MD
Kotaro Shimada, MD
Tomohisa Okada, MD, PhD
Toshiya Shibata, MD, PhD
Kaori Togashi, MD, PhD

Purpose: To evaluate the effectiveness of the periodically rotated overlapping parallel lines with enhanced reconstruction (PROPELLER) technique for superparamagnetic iron oxide (SPIO)-enhanced T2-weighted magnetic resonance (MR) imaging with respiratory compensation with the prospective acquisition correction (PACE) technique in the detection of hepatic lesions.

Materials and Methods: The institutional human research committee approved this prospective study, and all patients provided written informed consent. Eighty-one patients (mean age, 58 years) underwent hepatic 1.5-T MR imaging. Fat-saturated T2-weighted turbo spin-echo images were acquired with the PACE technique and with and without the PROPELLER method after administration of SPIO. Images were qualitatively evaluated for image artifacts, depiction of liver edge and intrahepatic vessels, overall image quality, and presence of lesions. Three radiologists independently assessed these characteristics with a five-point confidence scale. Diagnostic performance was assessed with receiver operating characteristic (ROC) curve analysis. Quantitative analysis was conducted by measuring the liver signal-to-noise ratio (SNR) and the lesion-to-liver contrast-to-noise ratio (CNR). The Wilcoxon signed rank test and two-tailed Student *t* test were used, and $P < .05$ indicated a significant difference.

Results: MR imaging with the PROPELLER and PACE techniques resulted in significantly improved image quality, higher sensitivity, and greater area under the ROC curve for hepatic lesion detection than did MR imaging with the PACE technique alone ($P < .001$). The mean liver SNR and the lesion-to-liver CNR were higher with the PROPELLER technique than without it ($P < .001$).

Conclusion: T2-weighted MR imaging with the PROPELLER and PACE technique and SPIO enhancement is a promising method with which to improve the detection of hepatic lesions.

[1] From the Department of Diagnostic Radiology, Kyoto University Graduate School of Medicine, 54 Shogoin Kawahara-cho, Sakyo-ku, Kyoto 606-8507, Japan. Received August 3, 2008; revision requested October 2; final revision received November 8; accepted December 1; final version accepted December 18. **Address correspondence to** Y.H. (e-mail: *yuusuke@kuhp.kyoto-u.ac.jp*).

Magnetic resonance (MR) imaging is one of the most useful methods with which to diagnose hepatic diseases. T2-weighted MR imaging playsan important role in the detection and characterization of hepatic lesions. Various MR imaging techniques have been investigated in an attempt to determine which method yields optimal T2-weighted images (1–4). Artifacts caused by respiratory motion are a major problem because they degrade image quality on T2-weighted MR images of the liver; therefore, most investigators have tried to acquire high-quality T2-weighted MR images without respiratory motion artifacts.

Breath-hold MR imaging with rapid acquisition can be used to effectively reduce respiratory motion artifacts and quickly obtain T2-weighted MR images of the liver in a short period of time (5,6). Turbo spin-echo (TSE) and half-Fourier rapid acquisition with relaxation enhancement sequences are widely used for breath-hold T2-weighted MR imaging, and they permit imaging of the entire liver during one or more breath holds (7–9). However, the use of multiple refocusing pulses during breath-hold T2-weighted imaging causes a decrease in the signal intensity of solid liver tumors due to the magnetization transfer effect, which can result in low conspicuity of malignant tumors (10,11). Another way to reduce respiratory motion artifacts is to use a respiratory triggering technique. This technique allows one to use shorter echo train length, more signal averaging, and higher spatial resolution, without being restricted by breath-hold time. This approach can result in a higher signal-to-noise ratio (SNR) and an improved liver-to-lesion contrast in comparison with those approaches involving breath-hold T2-weighted TSE or half-Fourier rapid acquisition with relaxation enhancement sequences (12–14). Hence, use of respiratory triggering is expected to improve the detection of focal hepatic solid lesions. Traditionally, a pneumatic belt has been wrapped around the abdomen to implement this technique (12); however, more recently, a method—navigator-triggered prospective acquisition correction (PACE)—has become available (15–17). This technique is used to directly observe superior-inferior movement of the diaphragm, and it is suitable for use with the respiratory triggering technique. Use of this technique resulted in better image quality than that attained with respiratory triggering with use of a pneumatic belt in coronary MR angiography (18). If available, PACE is the method of choice with which to reduce respiratory motion artifacts. However, use of this technique cannot completely eliminate image artifacts, and it may have variable performance in patients with irregular or shallow respiration.

The periodically rotated overlapping parallel lines with enhanced reconstruction (PROPELLER) technique (19) has been introduced into clinical practice (20–23). The PROPELLER technique, also referred to as the BLADE method (Siemens Medical Systems, Erlangen, Germany), is a variant of the radial imaging technique and enables correction of in-plane motion by using data acquired at the k-space center by every blade. PROPELLER MR imaging offers a substantial advantage over other techniques by providing targeted corrections for the major in-plane movements of rotation and translation. This method can be used with other techniques, such as PACE, for motion correction, and it yields a better SNR by oversampling data at the center of the k-space (19).

MR imaging with the PROPELLER technique has seen widespread clinical use in the brain; however, there have been only a few studies on its use in the upper abdomen (24–27). These earlier studies revealed a reduction in the number of motion artifacts on PROPELLER images; however, to our knowledge, a large prospective study on lesion detectability has not been conducted. The purpose of this study was to evaluate the effectiveness of the PROPELLER technique in superparamagnetic iron oxide (SPIO)-enhanced T2-weighted MR imaging with respiratory compensation with the PACE technique in the detection of hepatic lesions.

Advance in Knowledge

- T2-weighted MR imaging with the periodically rotated overlapping parallel lines with enhanced reconstruction (PROPELLER) and prospective acquisition correction (PACE) techniques after administration of superparamagnetic iron oxide (SPIO) is more sensitive and effective in the detection of both solid and nonsolid hepatic lesions than is imaging with the PACE technique alone after SPIO administration.

Implication for Patient Care

- The addition of the PROPELLER method to the PACE technique for SPIO-enhanced T2-weighted MR imaging enables improved detection of hepatic lesions.

Materials and Methods

Patients

The institutional review board approved this prospective study, and all patients provided written informed consent for

Published online
10.1148/radiol.2512081360

Radiology 2009; 251:388–397

Abbreviations:
A_z = area under the ROC curve
PACE = prospective acquisition correction
PROPELLER = periodically rotated overlapping parallel lines with enhanced reconstruction
ROC = receiver operating characteristic
SNR = signal-to-noise ratio
SPIO = superparamagnetic iron oxide
TSE = turbo spin echo

Author contributions:
Guarantor of integrity of entire study, Y.H.; study concepts/study design or data acquisition or data analysis/interpretation, all authors; manuscript drafting or manuscript revision for important intellectual content, all authors; manuscript final version approval, all authors; literature research, Y.H., T.S.; clinical studies, Y.H., S.A., K.S., K.T.; statistical analysis, Y.H.; and manuscript editing, Y.H., H.I., T.O., T.S.

Authors stated no financial relationship to disclose.

enrollment prior to MR imaging. From September 2007 to February 2008, 111 consecutive patients underwent SPIO-enhanced MR imaging to evaluate focal liver lesions. Thirteen patients were excluded for the following reasons: Six patients were excluded because they had contraindications to MR imaging (claustrophobia or a pacemaker); three were unable to receive SPIO because of hemochromatosis or hepatic insufficiency; and four were unable to provide informed consent. Hepatic MR imaging was performed to rule out metastases from pancreatic or colorectal tumors in 42 patients, as a follow-up examination for hepatocellular carcinoma in 27 patients, to rule out hepatocellular carcinoma in 18 patients with liver cirrhosis or chronic liver damage, and to evaluate focal hepatic lesions detected with computed tomography (CT) or ultrasonography (US) in 11 patients. Seventeen patients were excluded after they underwent MR imaging because the final diagnosis had not been established (n = 11), they had more than 10 lesions (n = 5), or there was a failure in respiratory compensation due to severe motion (n = 1). Thus, data from a total of 81 patients (mean age, 58 years; age range, 25–82 years)—43 men (mean age, 57 years; age range, 25–78 years) and 38 women (mean age, 60 years; age range, 28–82 years)—were analyzed.

MR Image Acquisition and Preparation

Upper abdominal MR imaging was performed with a 1.5-T system (Magnetom Symphony; Siemens Medical Systems) equipped with a six-channel phase-array body coil. After intravenous administration of SPIO (0.016 mL [8 μmol of iron] per kilogram of body weight for a maximum volume of 1.4 mL; Resovist, Bayer Schering Pharma, Osaka, Japan) over the course of 20 minutes, two sets of fat-saturated T2-weighted TSE images of the liver were obtained with the PACE technique. The two sets of images were the same except one set of images was acquired with the PROPELLER technique and the other was acquired without it (hereafter, PROPELLER and non-PROPELLER images, respectively). The PROPELLER technique is used to determine the number of blades that are rotated around the center of the k-space. The MR system required the width of the blade, which defines the phase-encoding lines per blade, to be more than 29 for motion correction. Each blade was evenly rotated 14 times to completely cover the k-space. Other parameters were the same for image acquisition with or without the PROPELLER technique and were as follows: 85-msec echo time, 150° flip angle, 425 Hz/pixel bandwidth, echo train length of 31, 32 × 32-cm field of view, 6-mm section thickness without an intersection gap, 256 × 256 matrix, and 1.25 × 1.25 × 6.00-mm voxel size. Image acquisition with the PROPELLER technique required a mean examination time of 300 seconds ± 59 (standard deviation), whereas image acquisition without the PROPELLER technique required a mean examination time of 222 seconds ± 45. Patients were asked to raise their arms outside the coils to ensure better image quality, and all patients were able to comply with this request.

One abdominal radiologist (Y.H., 12 years of experience) who did not participate in the data analysis removed any information related to the patient or examination technique and saved the images. He explained the method of assessment and presented image data sets at random to each evaluator, who was blinded to information on the subjects and the MR acquisition methods.

Image Data Analysis

All image data sets were presented at random and were evaluated independently by three experienced abdominal radiologists (H.I., Y.S.M., S.A.; 20, 17, and 8 years of experience, respectively) with a Digital Imaging and Communications in Medicine viewer (Centricity, version 2.0; GE Healthcare BioSciences, Tokyo, Japan). The evaluators were blinded to subject data and MR acquisition conditions, and they independently examined all MR image data sets (27 MR images per sequence), including both PROPELLER and non-PROPELLER images, obtained in each subject.

Image Quality

The readers graded image artifacts—such as ghosting and streaking (20,24), vascular pulsation, and peristalsis—with a five-point confidence scale (1, severe peristalsis; 2, moderate peristalsis; 3, mild peristalsis; 4, minimal peristalsis; 5, no peristalsis). Depiction of the liver edge and intrahepatic vessels was also assessed: A score of 1 indicated unacceptable depiction; a score of 2, poor and severely blurred depiction; a score of 3, moderate depiction; a score of 4, clear depiction with slight blurring; and a score of 5, excellent depiction with no blurring. Overall image quality was ranked as follows: A score of 1 indicated nondiagnostic image quality; a score of 2, poor image quality; a score of 3, fair image quality; a score of 4, good image quality; and a score of 5, excellent image quality. For each item evaluated, one score was given for one set of images from one subject, resulting in a total of six scores for three evaluation items for two T2-weighted image sets acquired with and without the PROPELLER technique.

Lesion Detection and Characterization

The same evaluators independently examined two MR image sets acquired with and without the PROPELLER technique in a randomized order, checked the total number of hepatic lesions per acquisition and the total number of patients at the same time, and recorded the presence of each visible abnormality with a five-point confidence scale (1, definitely or almost definitely absent; 2, probably absent; 3, possibly present; 4, probably present, and 5, definitely or almost definitely present). The evaluators then characterized each detected lesion with a five-point scale (1, definitely or almost definitely nonsolid; 2, probably nonsolid; 3, indeterminate consistency; 4, probably solid; and 5, definitely or predominantly solid). A nonsolid lesion was defined as a lesion with high and homogeneous signal intensity similar to that of fluid components, such as cerebrospinal fluid, on a

Table 1

Final Diagnosis and Method Used to Establish the Diagnosis in Hepatic Lesions

Final Diagnosis	Total No. of Lesions	Histologic Examination		Imaging
		Surgical Resection	US-guided Biopsy	
Solid lesions				
Hepatocellular carcinoma	58	45	0	13
Metastasis	48	17	2	29
Intrahepatic cholangiocarcinoma	3	3	0	0
Nonsolid lesions				
Hemangioma	21	4	0	17
Cyst	62	17	0	45

Note.—Data are numbers of lesions. Total sample size was 192 lesions in 81 patients.

Table 2

Image Quality of T2-weighted MR Images Obtained with and without the PROPELLER Technique

Observer and Image Quality Criteria	MR Imaging with the PROPELLER Technique	MR Imaging without the PROPELLER Technique	*P* Value*
Observer 1			
Image artifact	4.22 ± 0.46	2.18 ± 0.38	<.001
Depiction of liver edge and intrahepatic vessels	4.15 ± 0.43	2.35 ± 0.40	<.001
Overall image quality	4.05 ± 0.52	1.78 ± 0.28	<.001
Observer 2			
Image artifact	4.15 ± 0.43	1.95 ± 0.35	<.001
Depiction of liver edge and intrahepatic vessels	3.88 ± 0.34	2.02 ± 0.33	<.001
Overall image quality	3.75 ± 0.55	2.39 ± 0.32	<.001
Observer 3			
Image artifact	4.29 ± 0.48	2.47 ± 0.43	<.001
Depiction of liver edge and intrahepatic vessels	3.93 ± 0.42	2.11 ± 0.38	<.001
Overall image quality	3.88 ± 0.44	2.26 ± 0.35	<.001

Note.—Unless otherwise indicated, data are mean image quality scores ± standard deviations. Total sample size was 192 lesions in 81 patients.

* $P < .05$ indicates a significant difference.

Table 3

A_z Values for Detection of All Hepatic Lesions for Each Observer

Observer and Overall Mean	MR Imaging with the PROPELLER Technique	MR Imaging without the PROPELLER Technique	*P* Value*
1	0.91 ± 0.03	0.78 ± 0.04	<.001
2	0.88 ± 0.03	0.74 ± 0.03	<.001
3	0.90 ± 0.03	0.76 ± 0.04	<.001
Mean	0.90 ± 0.03	0.76 ± 0.04	<.001

Note.—Unless otherwise indicated, data are mean A_z values ± standard errors of the mean. Total sample size was 192 lesions in 81 patients.

* $P < .05$ indicates a significant difference.

T2-weighted image. A solid lesion was defined as a lesion with signal intensity lower than that of fluid. The evaluators also noted the segment in which they suspected the hepatic lesions were located. When multiple lesions were present, each suspected lesion was scored, and the segment in which it was located was noted.

Quantitative Analysis

Quantitative image analysis was performed by an experienced abdominal radiologist (K.S., 8 years of experience) who used operator-defined regions of interest (ROIs) to measure the signal intensity of the liver (SI_{liver}) and the focal liver lesion (SI_{lesion}) and the standard deviation of the background noise (SD_{noise}) for each image. This radiologist did not participate in qualitative image analysis and had no knowledge of patient information or imaging parameters. An abdominal radiologist (Y.H.) who had access to all the study information identified the target lesions for measurement. Signal intensity of the liver was measured in the same area, which was devoid of a large intrahepatic vessel or prominent artifacts, on images acquired with or without the PROPELLER technique. For all measurements, the size of the ROI was identical for both acquisition methods. Standard deviation of the background noise was measured in the largest possible circular ROI positioned in an area that was just ventral to the liver outside the patient along the phase-encoding direction. The area of the ROI in the focal liver lesions was positioned to maintain an ROI of at least 20 mm^2, while avoiding necrotic or scarring foci. Lesions smaller than 1 cm in diameter were excluded from quantitative analysis because it was difficult to avoid including the adjacent liver within the ROI. The ROI of the liver was drawn in the hepatic parenchyma near the lesions to exclude a vessel and image artifacts and was at least 80 mm^2 in all patients. Some hepatic lesions were also excluded from analysis because they were difficult to measure accurately owing to their small size and poor image quality. The liver SNR was calculated with the following equation:

Table 4

Sensitivity and Positive Predictive Value of MR Imaging with and without the PROPELLER Technique for Solid and Nonsolid Hepatic Lesions

A: Sensitivity of MR Imaging

Observer and Lesion Type	MR Imaging with the PROPELLER Technique		MR Imaging without the PROPELLER Technique		
	Sensitivity*	95% CI	Sensitivity*	95% CI	*P* Value†
Solid					
1	92 (100/109)	85, 96	75 (82/109)	66, 83	<.001
2	89 (97/109)	82, 94	72 (78/109)	62, 80	<.001
3	91 (99/109)	84, 96	73 (80/109)	64, 81	<.001
Nonsolid					
1	93 (77/83)	85, 97	84 (70/83)	75, 91	<.001
2	92 (76/83)	83, 97	82 (68/83)	72, 90	<.001
3	94 (78/83)	87, 98	84 (70/83)	75, 91	<.001
All lesions	92 (527/576)	89, 94	78 (448/576)	74, 81	<.001

B: Positive Predictive Value of MR Imaging

Observer and Lesion Type	MR Imaging with the PROPELLER Technique		MR Imaging without the PROPELLER Technique		
	Positive Predictive Value‡	95% CI	Positive Predictive Value‡	95% CI	*P* Value†
Solid					
1	97 (100/103)	92, 99	86 (82/95)	78, 93	<.001
2	96 (97/101)	90, 99	85 (78/92)	76, 91	<.001
3	96 (99/103)	90, 99	83 (80/96)	74, 90	<.001
Nonsolid					
1	98 (77/79)	91, 100	89 (70/79)	80, 95	<.001
2	96 (76/79)	89, 99	85 (68/80)	75, 92	<.001
3	98 (78/80)	91, 100	89 (70/79)	80, 95	<.001
All lesions	97 (527/545)	95, 98	86 (448/521)	83, 89	<.001

Note.—The total sample size was 192 lesions in 81 patients. CI = confidence interval.

* Data are percentages. Data in parentheses are those used to calculate sensitivity values.

† *P* values were calculated with the McNemar test. $P < .05$ indicates a significant difference.

‡ Data are percentages. Data in parentheses are those used to calculate positive predictive values.

$SNR = SI_{liver}/SD_{noise}$. The lesion-to-liver contrast-to-noise ratio (CNR) was calculated with the following equation: $CNR = (SI_{lesion} - SI_{liver})/SD_{noise}$.

Statistical Analysis

Each evaluator assessed image quality (image artifacts, depiction of liver edge and vessels, and overall image quality) with the Wilcoxon signed rank test by comparing scores for PROPELLER and non-PROPELLER image sets obtained in each patient. For analysis of lesion detection in the liver, an alternative free-response receiver operating characteristic (ROC) curve was fitted to each evaluator's confidence rating by using a maximum likelihood estimation program (ROCKIT, version 1.0.1 B2; C. E. Metz, University of Chicago, Chicago, Ill) for each image set acquired with or without PROPELLER acquisition. The diagnostic accuracy of each image set for each observer and the composite data were calculated by measuring the area under the ROC curve (A_z). Relative sensitivity for detection of lesions and differentiation of solid from nonsolid lesions was calculated for lesions with a score of 4 or 5. The differences between image sets in terms of the mean A_z value were analyzed with the two-tailed Student *t* test for paired data. The sensitivity for detection of hepatic lesions on a per-lesion basis and the positive predictive value for each image set were also calculated. The sensitivity and positive predictive value of PROPELLER and non-PROPELLER MR images were compared with the McNemar test. To assess interobserver variability in image interpretation, the κ statistic was used to measure the degree of agreement among multiple observers: A κ value of 0.00 implied poor agreement; a κ value of 0.01–0.20, slight agreement; a κ value of 0.21–0.40, fair agreement; a κ value of 0.41–0.60, moderate agreement; a κ value of 0.61–0.80, substantial agreement; and a κ value of 0.81–1.00, almost perfect agreement. The liver SNR and the lesion-to-liver contrast-to-noise ratio were compared between the image

sets by using linear mixed models. $P < .05$ was considered to indicate a significant difference. Statistical analysis was performed with statistical software (SPSS, version 15.0; SPSS, Chicago, Ill).

Results

Lesion Characteristics

All available data in the form of pathologic specimens, image characteristics, and clinical courses were reviewed and revealed that 57 patients had a total of 192 focal hepatic lesions (five patients had only nonsolid lesions) and 24 patients had no focal hepatic lesions (Table 1). Hepatic lesions included 83 nonsolid (mean diameter, 2.9 cm; range, 0.4–6.6 cm) and 109 solid (mean diameter, 4.3 cm; range, 0.5–10.8 cm) lesions. Of the 83 nonsolid lesions, diagnoses of hemangioma ($n = 21$) and cyst ($n = 62$) were mainly based on the characteristic findings of contrast material–enhanced CT, gadolinium-enhanced MR imaging, or US; however, 21 of these diagnoses (four hemangiomas, 17 cysts) were pathologically confirmed at resection. Of the 109 solid lesions, 58 were hepatocellular carcinomas, 48 were metastases, and three were intrahepatic cholangiocarcinomas. Of the 58 hepatocellular carcinomas in 30 patients, 45 lesions in 26 patients were pathologically confirmed at surgical resection. The remaining 13 hepatocellular carcinomas in four patients were diagnosed by virtue of the characteristic enhancement pattern on dynamic CT or MR images and uptake of the iodized oil by the lesion on CT images after transarterial chemoembolization. Of the 48 metastases, 17 were confirmed at surgical resection in 11 patients, and two were confirmed at US-guided biopsy in two patients. The remaining 29 metastases in seven patients were diagnosed by virtue of typical findings on contrast-enhanced CT and SPIO-enhanced MR images, and the interval growth of hepatic lesions on follow-up images enabled us to confirm this finding. Three other hepatic lesions in two patients were diagnosed as intrahepatic cholangiocarcinomas at surgical resection.

Table 5

Interobserver Agreement with Regard to Hepatic Lesions

Observer, Lesion Type, and Overall Mean	MR Imaging with the PROPELLER Technique	MR Imaging without the PROPELLER Technique
Solid lesion		
Observer 1 vs observer 2	0.72 ± 0.04	0.62 ± 0.05
Observer 2 vs observer 3	0.77 ± 0.03	0.66 ± 0.04
Observer 1 vs observer 3	0.81 ± 0.03	0.73 ± 0.04
Nonsolid lesion		
Observer 1 vs observer 2	0.83 ± 0.03	0.64 ± 0.04
Observer 2 vs observer 3	0.73 ± 0.04	0.63 ± 0.04
Observer 1 vs observer 3	0.72 ± 0.04	0.76 ± 0.03
Overall mean	0.76 ± 0.04	0.67 ± 0.04

Note.—Data are mean κ values ± standard errors of the mean. The total sample size was 192 lesions in 81 patients.

Image Quality

Comparative visual assessments showed image artifact, depiction of liver edge and intrahepatic vessels, and overall image quality were significantly better for all observers on T2-weighted MR

Figure 1

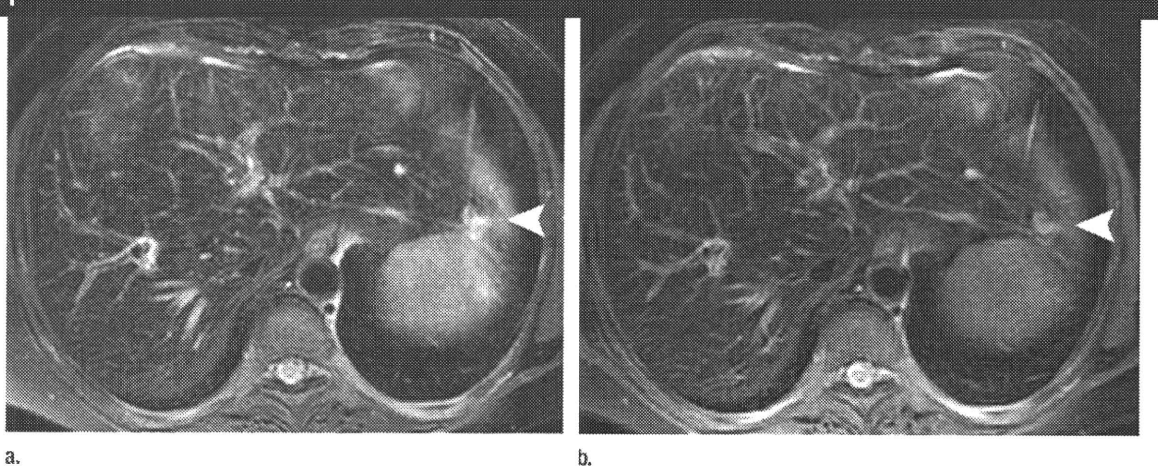

a. b.

Figure 1: Fat-saturated T2-weighted TSE axial MR images obtained after SPIO administration with respiratory triggering in a 62-year-old man with pancreatic cancer. **(a)** Image acquired with the PACE method alone shows a metastatic lesion (arrowhead) at the edge of the left hepatic lobe obscured by image artifacts. **(b)** The hepatic lesion (arrowhead) can be seen more clearly on the PROPELLER MR image.

Figure 2

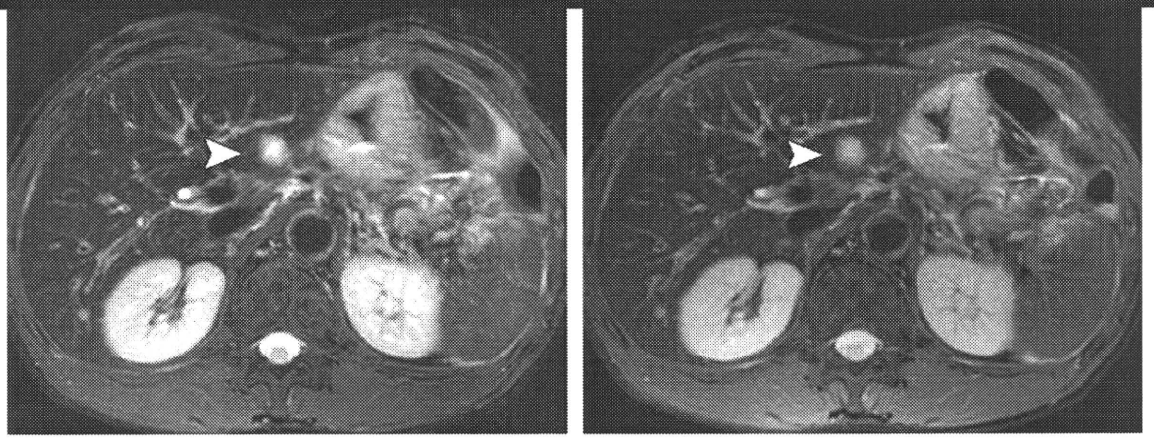

a. b.

Figure 2: Fat-saturated T2-weighted TSE axial MR images obtained after SPIO administration with respiratory triggering in a 48-year-old woman with hepatocellular carcinoma. **(a)** Image acquired with the PACE method alone depicts the hepatic tumor (arrowhead) in segment II less clearly than in **b** because of ghosting artifacts; however, a hepatic cyst in segment IV is apparent. **(b)** The hepatic tumor (arrowhead) in segment II is clearly visible on the PROPELLER MR image.

Figure 3

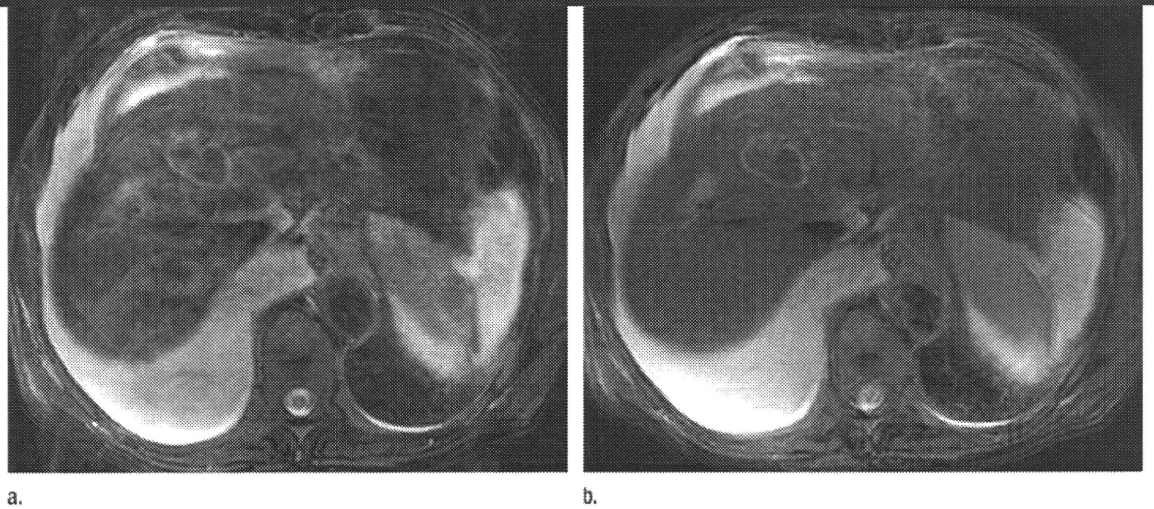

a. b.

Figure 3: Follow-up fat-saturated T2-weighted TSE axial MR images obtained after SPIO administration with respiratory triggering in a 55-year-old woman with hepatocellular carcinoma, liver cirrhosis, and ascites. **(a)** Image acquired with the PACE method alone shows that it is difficult to evaluate hepatic lesions in detail because of poor image quality. **(b)** In addition to the posttherapeutic (radiofrequency ablation) hepatic lesion for hepatocellular carcinoma in segments IV and VIII, the PROPELLER MR image clearly shows a solid hepatic lesion suspected to be the recurrent hepatocellular carcinoma in segment VIII.

images obtained with the PROPELLER technique than on those obtained without it (Table 2).

Lesion Detection and Characterization

The mean A_z values ± standard errors for each observer in the detection of hepatic lesions as a whole are summarized in Table 3. For all observers, the individual and mean A_z values for PROPELLER images were significantly greater than those for non-PROPELLER images, regardless of the order of data sets and MR images. The sensitivity for detection and characterization of hepatic lesions and the positive predictive value of MR imaging with the PROPELLER technique were superior to those of MR imaging without the PROPELLER technique in solid and nonsolid lesions (Table 4). Interobserver agreement was high for both methods of MR image acquisition (Table 5). Fourteen lesions were not

detected by any observer with either technique. Nine of these lesions (solid, $n = 6$; nonsolid, $n = 3$) were smaller than 1.0 cm in diameter (0.3–0.9 cm), and the remaining five (solid, $n = 3$; nonsolid, $n = 2$) had little contrast with the surrounding liver parenchyma. The nine lesions smaller than 1.0 cm in diameter were diagnosed with gadolinium-enhanced MR imaging (two solid lesions), contrast-enhanced multidetector CT (two solid lesions, one nonsolid lesion), or contrast-enhanced US (two nonsolid lesions) or on the basis of enlargement at follow-up examinations (two solid lesions). The five lesions that had little contrast with the surrounding liver parenchyma were diagnosed at contrast-enhanced multidetector CT (one solid lesion, two nonsolid lesions) or contrast-enhanced US (two solid lesions). Examples of the advantages of PROPELLER MR imaging are presented in Figures 1–3.

Quantitative Analysis

A total of 21 nonsolid lesions and 25 solid lesions in 18 patients were smaller than 1 cm in diameter and were excluded from quantitative analysis. Furthermore, two nonsolid and three solid lesions in two patients were also excluded from this analysis because the images acquired with only the PACE method were of poor quality. Of these lesions, one nonsolid lesion and two solid lesions in one patient were of poor quality on T2-weighted images acquired with both the PROPELLER technique and the PACE technique. An additional nine lesions (four nonsolid lesions, five solid lesions) in two patients were not detected with or without the PROPELLER method, although image quality was not poor. For the remaining 56 nonsolid lesions and 76 solid lesions in 39 patients, the mean liver SNR and the lesion-to-liver contrast-to-noise ratio were significantly higher for MR imaging with the PROPELLER technique than for MR imaging without the PROPELLER technique (Table 6).

Discussion

MR imaging with SPIO is currently used to improve the detection and characterization of focal hepatic lesions (28–31). Investigators have adapted various pulse sequences for SPIO-enhanced MR imaging and have compared imaging sequences (32,33). Ishiyama et al reported that respiratory-triggered T2-weighted TSE images provided greater tumor-to-liver contrast and subjective conspicuity for hepatic lesions after SPIO administration (34). However, artifacts such as respiratory motion, cardiovascular pulsation, bowel movement, and physical movement resulted in deterioration of abdominal MR image quality and, consequently, the detection of abdominal lesions was impaired (35–37). To overcome these problems, the PROPELLER technique, which has the advantage of central k-space oversampling and the capability of motion correction, would be expected to not only reduce image artifacts but also contribute to better SNR and lesion detection (19).

Preliminary evaluations of PROPELLER MR imaging in the abdomen were reported in three patients by Deng et al (25) and in 14 patients by Kiryu et al (24). In the latter report, respiratory triggering was applied with a pneumatic belt; however, motion artifacts were noted in two patients because of the intrinsic inaccuracy of this technique. In a previous study, MR imaging with the PROPELLER and PACE techniques was shown to reduce image artifacts and noise and to produce better image quality in the upper abdomen (26). These results suggested the possibility of improved detection of hepatic lesions with adoption of these methods. The results of our qualitative analysis were in concordance with this prediction and showed that the detection of both solid and nonsolid hepatic lesions with the PROPELLER and PACE techniques was superior to that with the PACE method alone. When only the PACE method was used, it was sometimes difficult to diagnose lesions in the subdiaphragm or liver edge because of image artifacts caused by an irregular respiratory rhythm; however, use of the PACE method improved image quality and enabled thin-section examinations to be performed with an even thinner section thickness (16). The PROPELLER technique, which is a variant of the radial imaging techniques, did not generate ghosting artifacts (26). This consequently helped in the detection of abdominal lesions that were obscured by ghosting artifacts on PACE images.

Our quantitative results show that MR imaging with the PROPELLER technique resulted in a higher SNR in the liver and a higher lesion-to-liver contrast-to-noise ratio than did MR imaging without the PROPELLER technique. Although data collection with the PROPELLER technique requires an additional factor of $\pi/2$ imaging time over that of conventional examinations to cover the entire k-space, it results in an increased SNR (19), which is likely to have contributed to the improvement in abdominal lesion detection (38). The average imaging time was longer for MR imaging with the PROPELLER technique than for MR imaging without the PROPELLER technique because the former requires approximately 60% more time to cover the entire k-space (19). This might have

Table 6

Quantitative Analysis of MR Imaging with and without the PROPELLER Technique

Parameter	MR Imaging with the PROPELLER Technique	MR Imaging without the PROPELLER Technique	*P* Value*
Liver SNR	36.4 ± 17.8	23.7 ± 11.2	<.001
Lesion-to-liver contrast-to-noise ratio	54.9 ± 31.0	38.2 ± 20.7	<.001
Solid lesion	37.6 ± 25.4	24.2 ± 17.5	<.001
Nonsolid lesion	78.4 ± 38.6	57.2 ± 25.1	<.001

Note.— Data are means ± standard deviations. The total sample size was 56 nonsolid lesions and 76 solid lesions in 39 patients.

* $P < .001$ indicates a significant difference.

contributed to the better SNR we observed; however, the amount of improvement due to the longer acquisition time is limited because SNR increases to the square root of the increased time. The large increases in SNR and contrast-to-noise ratio are considered to be due to the reduction of widespread motion artifact that resulted from use of the PROPELLER method.

T2-weighted MR imaging provides additional diagnostic information, and it can help characterize focal lesions, especially nonsolid lesions, such as cysts or hemangiomas (38,39). PROPELLER MR imaging after SPIO administration can improve the detection of hepatic lesions.The sensitivity and positive predictive value for detection and characterization of hepatic lesions with the PROPELLER method were significantly higher than those without the PROPELLER method. The PROPELLER MR technique was effective in depicting a variety of hepatic lesions and was used to differentiate solid lesions from nonsolid lesions. MR imaging with the PACE method alone resulted in more false-positive and false-negative findings because of poor image quality and image artifacts.

Our study had several potential limitations. First, our reference standard was not completely optimal for hepatic lesion detection and characterization. However, a more rigorous standard, such as full pathologic confirmation, was not applicable for all patients, especially those with benign lesions. Second, more image reconstruction time was required with the PROPELLER technique than with the PACE method alone. This caused some delay in imaging; however, it is expected that the reconstruction speed will decrease in the future through technologic advances. Third, the parameters for PROPELLER acquisition were not fully investigated and may not have been optimal. Fourth, PROPELLER MR imaging with other contrast agents and sequences was not evaluated; however, this should be examined in the future to improve detection of lesions. Fifth, parallel acquisition techniques that would reduce the acquisition time were not used in our study.

In summary, T2-weighted MR imaging with the PROPELLER and PACE technique with SPIO enhancement is a promising method for improving hepatic lesion detection. Future clinical studies are required to further evaluate abdominal MR imaging with the optimized PROPELLER technique.

References

1. Bailes DR, Gilderdale DJ, Bydder GM, Collins AG, Firmin DN. Respiratory ordered phase encoding (ROPE): a method for reducing respiratory motion artefacts in MR imaging. J Comput Assist Tomogr 1985;9:835–838.
2. Ehman RL, McNamara MT, Pallack M, Hricak H, Higgins CB. Magnetic resonance imaging with respiratory gating: techniques and advantages. AJR Am J Roentgenol 1984; 143:1175–1182.
3. Haacke EM, Lenz GW. Improving MR image quality in the presence of motion by using rephasing gradients. AJR Am J Roentgenol 1987;148:1251–1258.
4. Hinks RS, Constable RT. Gradient moment nulling in fast spin echo. Magn Reson Med 1994;32:698–706.
5. Reinig JW. Breath-hold fast spin-echo MR imaging of the liver: a technique for high-quality T2-weighted images. Radiology 1995; 194:303–304.
6. Gaa J, Hatabu H, Jenkins RL, Finn JP, Eldelmann RR. Liver masses: replacement of conventional T2-weighted spin echo MR imaging with breath-hold MR imaging. Radiology 1996;200:459–464.
7. Outwater EK, Mitchell DG, Vinitski S. Abdominal MR imaging: evaluation of a fast spin-echo sequence. Radiology 1994;190: 425–429.
8. Yu JS, Kim KW, Kim YH, Jeong EK, Chien D. Comparison of multishot turbo spin echo and HASTE sequences for T2-weighted MRI of liver lesions. J Magn Reson Imaging 1998; 8:1079–1084.
9. Lee MG, Jeong YK, Kim JC, et al. Fast T2-weighted liver MR imaging: comparison among breath-hold turbo-spin-echo, HASTE, and inversion recovery (IR) HASTE sequences. Abdom Imaging 2000;25:93–99.
10. Outwater E, Schnall MD, Braitman LE, Dinsmore BJ, Kressel HY. Magnetization transfer of hepatic lesions: evaluation of a novel contrast technique in the abdomen. Radiology 1992;182:535–540.
11. Ichikawa T, Araki T. Fast magnetic resonance imaging of liver. Eur J Radiol 1999;29: 186–210.
12. Low RN, Alzate GD, Shimakawa A. Motion suppression in MR imaging of the liver: comparison of respiratory-triggered and nontriggered fast spin-echo sequences. AJR Am J Roentgenol 1997;168:225–231.
13. Pauleit D, Textor J, Bachmann R, et al. Improving the detectability of focal liver lesions on T2-weighted MR images: ultrafast breath-hold or respiratory-triggered thin-section MRI? J Magn Reson Imaging 2001;14:128–133.
14. Kanematsu M, Hoshi H, Itoh K, et al. Focal hepatic lesion detection: comparison of four fat-suppressed T2-weighted MR imaging pulse sequences. Radiology 1999;211: 363–371.
15. Zech CJ, Herrmann KA, Huber A, et al. High-resolution MR-imaging of the liver with T2-weighted sequences using integrated parallel imaging: comparison of prospective motion correction and respiratory triggering. J Magn Reson Imaging 2004;20:443–450.
16. Klessen C, Asbach P, Kroencke TJ, et al. Magnetic resonance imaging of the upper abdomen using a free-breathing T2-weighted turbo spin echo sequence with navigator triggered prospective acquisition correction. J Magn Reson Imaging 2005;21:576–582.
17. Asbach P, Klessen C, Kroencke TJ, et al. Magnetic resonance cholangiopancreatography using a free-breathing T2-weighted turbo spin-echo sequence with navigator-triggered prospective acquisition correction. Magn Reson Imaging 2005;23:939–945.
18. McConnell MV, Khasgiwala VC, Savord BJ, et al. Comparison of respiratory suppression methods and navigator locations for MR coronary angiography. AJR Am J Roentgenol 1997;168:1369–1375.
19. Pipe JG. Motion correction with PROPELLER MRI: application to head motion and free-breathing cardiac imaging. Magn Reson Med 1999;42:963–969.
20. Wintersperger BJ, Runge VM, Biswas J, et al. Brain magnetic resonance imaging at 3 tesla using BLADE compared with standard rectilinear data sampling. Invest Radiol 2006;41:586–592.
21. Forbes KP, Pipe JG, Bird CR, Heiserman JE. PROPELLER MRI: clinical testing of a novel technique for quantification and compensation of head motion. J Magn Reson Imaging 2001;14:215–222.
22. Forbes KP, Pipe JG, Karis JP, Heiserman JE. Improved image quality and detection of acute cerebral infarction with PROPELLER

diffusion-weighted MR imaging. Radiology 2002;225:551–555.

23. Forbes KP, Pipe JG, Karis JP, Farthing V, Heiserman JE. Brain imaging in the unsedated pediatric patient: comparison of periodically rotated overlapping parallel lines with enhanced reconstruction and single-shot fast spin-echo sequences. AJNR Am J Neuroradiol 2003;24:794–798.
24. Kiryu S, Watanabe M, Kabasawa H, Akahane M, Aoki S, Ohtomo K. Evaluation of super paramagnetic iron oxide-enhanced diffusion-weighted PROPELLER T2-fast spin echo magnetic resonance imaging: preliminary experience. J Comput Assist Tomogr 2006;30:197–200.
25. Deng J, Miller FH, Salem R, Omary RA, Larson AC. Multishot diffusion-weighted PROPELLER magnetic resonance imaging of the abdomen. Invest Radiol 2006;41:769–775.
26. Hirokawa Y, Isoda H, Maetani Y, Arizono S, Shimada K, Togashi K. MR image artifact reduction and quality improvement in the upper abdomen with the PROPELLER (BLADE) and navigator triggered prospective acquisition correction (PACE) technique. AJR Am J Roentgenol 2008;191:1154–1158.
27. Hirokawa Y, Isoda H, Maetani Y, Arizono S, Shimada K, Togashi K. Evaluation of motion correction effect and image quality with the PROPELLER (BLADE) and parallel imaging acquisition technique in the upper abdomen. J Magn Reson Imaging 2008;28:957–962.
28. Winter TC 3rd, Freeny PC, Nghim HV, et al. MR imaging with i.v. superparamagnetic iron oxide: efficacy in the detection of focal hepatic lesions. AJR Am J Roentgenol 1993;161:1191–1198.
29. Bellin MF, Zaim S, Auberton E, et al. Liver metastases: safety and efficacy of detection with superparamagnetic iron oxide in MR imaging. Radiology 1994;193:657–663.
30. Yamamoto H, Yamashita Y, Yoshimatsu S, et al. Hepatocellular carcinoma in cirrhotic livers: detection with unenhanced and iron oxide–enhanced MR imaging. Radiology 1995;195:106–112.
31. Schwartz LH, Seizer SE, Tempany CM, et al. Superparamagnetic iron oxide hepatic MR imaging: efficacy and safety using conventional and fast spin-echo pulse sequences. J Magn Reson Imaging 1995;5:566–570.
32. Van Beers BE, Lacrosse M, Jamart J, et al. Detection and segmental location of malignant hepatic tumors: comparison of ferumoxides-enhanced gradient-echo and T2-weighted spin-echo MR imaging. AJR Am J Roentgenol 1997;168:713–717.
33. Ward J, Guthrie JA, Wilson D, et al. Colorectal hepatic metastases: detection with SPIO-enhanced breath-hold MR imaging—comparison of optimized sequences. Radiology 2003;228:709–718.
34. Ishiyama K, Hashimoto M, Izumi J, et al. Tumor-liver contrast and subjective tumor conspicuity of respiratory-triggered T2-weighted fast spin-echo sequence compared with T2*-weighted gradient recalled-echo sequence for ferucarbotran-enhanced magnetic resonance imaging of hepatic malignant tumors. J Magn Reson Imaging 2008;27:1322–1326.
35. Wood ML, Henkelmann RM. MR image artifacts from periodic motion. Med Phys 1985;12:143–151.
36. Haacke EM, Patric JL. Reducing motion artifacts in two-dimensional Fourier transform imaging. Magn Reson Imaging 1986;4:359–376.
37. Yang W, Smith MR. Using an MRI distortion transfer function to characterize the ghosts in motion-corrupted images. IEEE Trans Med Imaging 2000;19:577–584.
38. Kim BS, Kim JH, Choi GM, et al. Comparison of three free-breathing T2-weighted MRI sequences in the evaluation of focal liver lesions. AJR Am J Roentgenol 2008;190:W19–W27.
39. Lee SS, Byun JH, Hong HS, et al. Image quality and focal lesion detection on T2-weighted MR imaging of the liver: comparison of two high-resolution free-breathing imaging techniques with two breath-hold imaging techniques. J Magn Reson Imaging 2007;26:323–330.

Spin-echo T1-weighted Imaging of the Brain with Interleaved Acquisition and Presaturation Pulse at 3 T:

A Feasibility Study Before Clinical Use[1]

Seiko Kasahara, MD, Yukio Miki, MD, PhD, Nobuyuki Mori, MD, Shin-ichi Urayama, PhD, Mitsunori Kanagaki, MD, PhD, Yasutaka Fushimi, MD, PhD, Chikara Maeda, MD, Nobukatsu Sawamoto, MD, PhD, Hidenao Fukuyama, MD, PhD, Kaori Togashi, MD, PhD

Rationale and Objectives. Although spin-echo (SE) sequence has some advantages over gradient-echo sequence in brain imaging, gradient-echo sequence is commonly used for T1-weighted imaging (T1WI) at 3 T because contrast on SE T1WI is widely believed to be poor at 3 T. Recently, gray-white matter contrast on single-slice and multi-slice SE imaging with interslice gap was reported as better at 3 T than at 1.5 T. This study examined the feasibility of interleaved SE T1WI of the brain at 3 T. This study also examined whether presaturation pulse (PP) sufficiently suppresses intra-arterial signals because these signals tend to be hyperintense due to longer T1 at 3 T.

Materials and Methods. Subjects consisted of 18 healthy volunteers. Two sets of T1WI were performed using SE sequence. One set consisted of imaging without PP, and the other consisted of imaging with PP. Each set contained three types of gapless imaging as follows; sequential, 100% interleaved, and 200% interleaved imaging. In each subject, contrast-to-noise ratio between gray-matter and white-matter ($CNR_{GM\text{-}WM}$) and intra-arterial signals were evaluated.

Results. $CNR_{GM\text{-}WM}$ was significantly higher on interleaved images than on sequential images, regardless of PP ($P < .0001$). PP sufficiently suppressed intra-arterial signals ($P < .0001$).

Conclusion. $CNR_{GM\text{-}WM}$ on SE T1WI at 3 T can be improved by interleaved acquisition, and PP sufficiently suppressed intra-arterial signals. Interleaved SE T1WI with PP appears clinically feasible at 3 T.

Key Words. Spin-echo sequence; T1-weighted image; brain; 3 T.

Gradient-echo (GRE) magnetic resonance (MR) sequences, such as magnetization-prepared rapid acquisition gradient echo and spoiled gradient echo, are commonly used for T1-weighted imaging at 3 T (1,2), since the contrast between gray matter (GM) and white matter (WM) on spin-echo (SE) T1-weighted imaging is widely believed to be lower at 3 T than at 1.5 T (2–5). On the other hand, some reports assessed a better contrast-to-noise ratio at 3 T by using optimized parameters on SE T1-weighted sequence (6,7).

SE sequence has several advantages in use for T1-weighted imaging. One is that magnetic susceptibility artifacts are less prominent on SE sequence than on GRE sequence (8). Another advantage of SE sequence is that patent intra-arterial lumens appear hypointense ("flow-void") on SE images, which enable differentiation between patent lumens and subacute intraluminal clots. On the other hand, GRE sequence appears not only intra-arterial subacute clots but also patent intra-arterial lumens as hyperintensity, so

Acad Radiol 2009; 16:852–857

[1] From the Department of Diagnostic Imaging and Nuclear Medicine (S.K., Y.M., N.M., M.K., C.M., K.T.) and Human Brain Research Center (S.U., N.S., H.F.), Graduate School of Medicine, Kyoto University, 54 Shogoin-Kawaharacho, Sakyo-ku, Kyoto 606-8507, Japan; and Department of Radiology, Hikone Municipal Hospital, Shiga, Japan (Y.F.). Received October 17, 2008; accepted December 30, 2008. **Address correspondence to:** Y.M. e-mail: mikiy@kuhp.kyoto-u.ac.jp

doi:10.1016/j.acra.2008.12.026

intra-arterial subacute clots could be easily missed on GRE (9). GRE imaging alone should not be used to determine the patency of aneurysms or cerebral arteriovenous malformations in the absence of corroborative images, particularly SE sequence (9). We recently demonstrated that contrast between GM and WM on single-slice SE T1-weighted MR images is better at 3 T than at 1.5 T (10). Moreover, we revealed that the influence of multi-slice imaging on contrast between GM and WM is significantly higher at 3 T than at 1.5 T, and suggested that SE T1-weighted imaging may be applicable at 3 T with sufficient interslice gap.

The present study examined differences in GM-WM contrast between sequential and interleaved SE T1-weighted imaging. Additionally, presaturation pulse (PP) was applied to suppress intra-arterial lumens (11), since intra-arterial lumens on T1-weighted imaging may tend to be hyperintense by paradoxical enhancement due to longer T1 relaxation time at 3 T. The present study also examined whether PP can sufficiently suppress intra-arterial signals. We therefore aimed to show that interleaved SE sequence with PP is feasible for acquisition of T1-weighted images of the brain with sufficient GM-WM contrast and sufficient suppression of intra-arterial signals.

MATERIALS AND METHODS

Subjects

Subjects comprised 18 volunteers (10 men, 8 women; mean age, 29 years; range, 24–38 years). All subjects were neurologically examined by a neurologist (N.S.) and were considered neurologically healthy. Each subject provided written informed consent.

Imaging Protocols

Whole brain scanning was performed using a 3 T MR scanner (Magnetom Trio; Siemens, Erlangen, Germany) using an 8-channel head coil. The head of the subject was fixed by means of a foam pad within the head coil, and subjects were instructed not to move during MR acquisition.

T1-weighted imaging was performed using SE sequence with: repetition time (TR), 600 ms; echo time (TE), 7.5 ms; slice thickness, 5 mm; number of averages, 1; number of slices, 24; matrix size, 256 × 256; flip angle, 90°; bandwidth, 190 Hz. One acquisition scheme consisted of images without PP, and the other consisted of images with PP; 50 mm-thick PP band was applied 10 mm below the imaging field. Each acquisition scheme contained three types of gapless images: sequential, 100% interleaved, and 200% interleaved imaging (Fig 1). Scan times were as follows: total sampling times were 158 s for sequential image, 314 s for 100% interleaved images (one interleaved acquisition sampling time was 157 s), and 450 s for 200% interleaved images (one interleaved acquisition sampling time was 150 s), respectively. Scan times were almost the same between acquisition scheme without PP and with PP at the same type of gapless image. Specific absorption rates of all acquisitions were within Food and Drug Administration guideline limits (12).

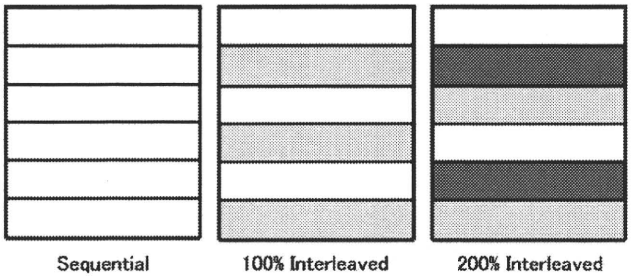

Figure 1. Illustration of acquisition schemes.

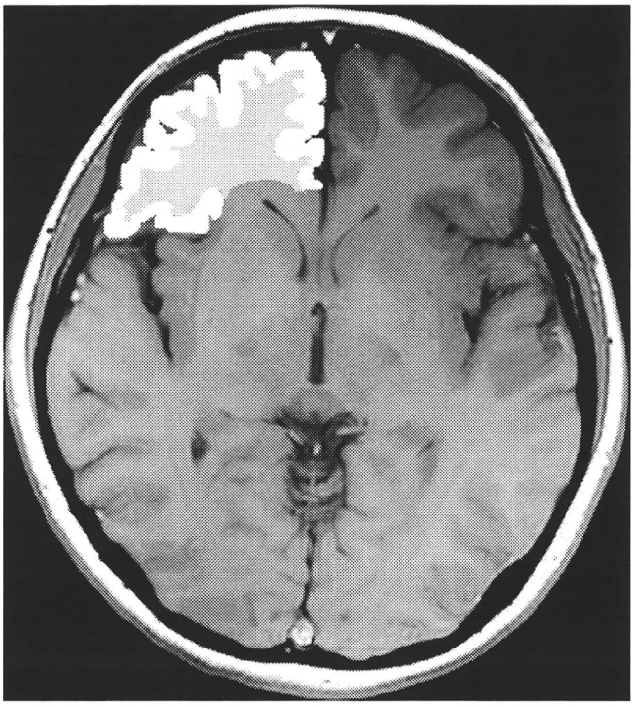

Figure 2. Representative image of a region-of-interest (ROI) on spin-echo T1-weighted imaging. Areas of gray matter and white matter in the frontal lobes were selected as ROIs.

Analysis of Contrast-to-Noise Ratio (CNR)

GM and WM of the right frontal lobe and background were manually selected as regions-of-interest (ROIs) at the level of the basal ganglia (Fig 2), according to a previous study (10). ROIs of the background signal were carefully placed so that ghost artifacts along the phase-encoding direction were not included. In each subject, the same ROIs were evaluated and CNR between GM and WM ($CNR_{GM\text{-}WM}$) was calculated as the difference between signal intensities (SI) of GM and WM

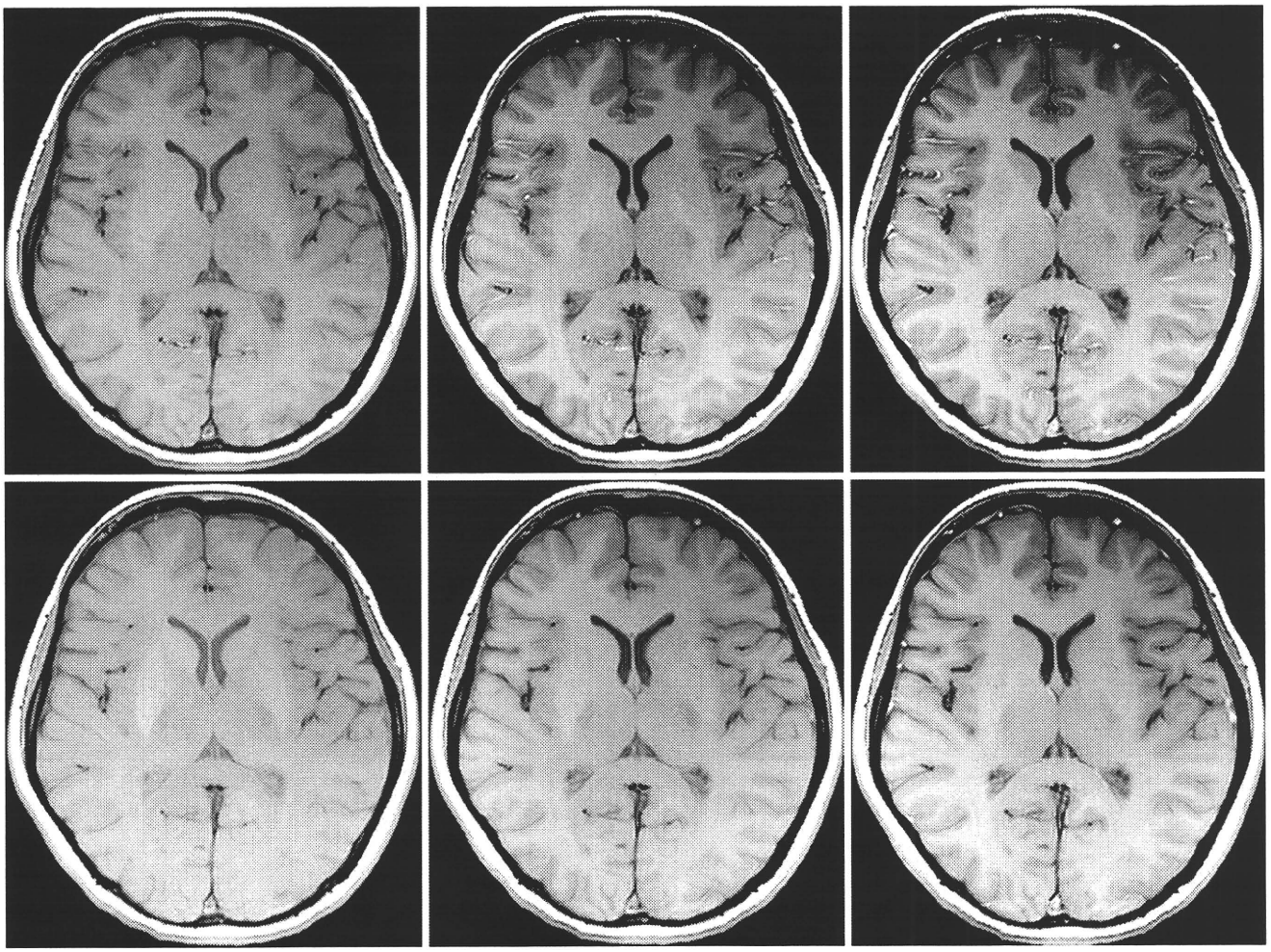

Figure 3. Spin-echo T1-weighted gapless multi-slice imaging without presaturation pulse (PP) (*upper row*) and with PP (*lower row*) at the level of the basal ganglia. From left to right, sequential imaging, 100% interleaved imaging, and 200% interleaved imaging are displayed. Gray matter and white matter contrast was more conspicuous with either 100% or 200% interleaved imaging than with sequential imaging.

divided by the standard deviation (SD) of the background: $| SI_{GM} - SI_{WM} |/SD_{background}$ (10). ROIs were drawn using ImageJ ver. 1.37 software (National Institutes of Health, Bethesda, MD).

Differences in $CNR_{GM\text{-}WM}$ among sequential images, 100% interleaved images, and 200% interleaved images were statistically analyzed by one-way repeated-measures analysis of variance for each acquisition scheme. Differences among means were then analyzed using post-hoc Tukey-Kramer multiple comparisons testing. Values of $P < .05$ were considered statistically significant. In addition, $CNR_{GM\text{-}WM}$ differences between acquisition schemes without PP and with PP in each of the three types of images (sequential, 100% interleaved, and 200% interleaved) were analyzed by paired *t*-tests. Values of $P < .05$ were considered statistically significant. Statistical analyses were performed using JMP ver. 5.1 software (SAS Institute, Cary, NC).

Analysis of Intra-arterial Signal

To evaluate the effect of PP on intra-arterial signals, those in the vertebral and basilar arteries were visually assessed by two independent, experienced neuroradiologists. These arteries were selected because they run in a vertical direction to the image plane and because they are frequent sites of dissection. Intra-arterial signals were expressed as: grade 0, no signal; grade 1, mixed signals; and grade 2, entirely hyperintense signal. If discrepancies existed between the two readers, consensus was obtained in discussion after both reading sessions were completed. Differences in grade of intra-arterial signals on the two acquisition schemes with and without PP were statistically assessed with Wilcoxon's

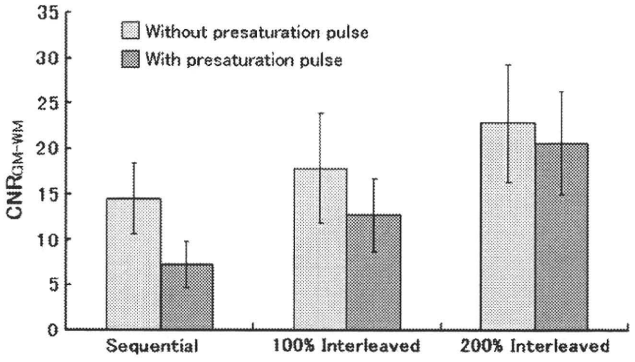

Figure 4. Contrast-to-noise ratio between gray-matter and white-matter (CNR_{GM-WM}) of sequential, 100% interleaved, and 200% interleaved imaging. Light gray, without presaturation pulse (PP); dark gray, with PP. Error bars represent standard deviations. Without PP, CNR_{GM-WM} for sequential, 100% interleaved, and 200% interleaved imaging was 14.48 ± 3.90, 17.85 ± 6.04, and 22.80 ± 6.56, respectively. With PP, CNR_{GM-WM} for sequential, 100% interleaved, and 200% interleaved imaging was 7.21 ± 2.57, 12.70 ± 4.04, and 20.61 ± 5.67, respectively.

signed rank test using JMP ver. 5.1 software. Values of $P < .05$ were considered statistically significant.

Institutional review board approval was obtained for this study.

RESULTS

On acquisition without PP, CNR_{GM-WM} of sequential, 100% interleaved, and 200% interleaved imaging was 14.48 ± 3.90, 17.85 ± 6.04, and 22.80 ± 6.56, respectively, showing significant differences ($P < .0001$). Post-hoc Tukey-Kramer multiple comparisons revealed a significant difference in CNR between sequential imaging and 100% interleaved imaging, and between sequential imaging and 200% interleaved imaging ($P < .01$). On acquisition scheme with PP, CNR_{GM-WM} of sequential, 100% interleaved, and 200% interleaved imaging was 7.21 ± 2.57, 12.70 ± 4.04, and 20.61 ± 5.67, respectively, representing a significant difference ($P < .0001$). Post-hoc Tukey-Kramer multiple comparisons testing revealed a significant difference among all imaging schemes ($P < .01$) (Figs 3 and 4). Application of PP significantly reduced CNR_{GM-WM} for all three imaging schemes ($P < .0001$ for sequential imaging, $P < .0001$ for 100% interleaved imaging, and $P = .0431$ for 200% interleaved imaging). CNR_{GM-WM} reduction rate by the application of PP on sequential, 100% interleaved, and 200% interleaved imaging was 50.21%, 28.85%, and 9.61%, respectively.

The effects of PP on vertebral and basilar intra-arterial signals are summarized in Table 1. On acquisition schemes without PP, vertebral intra-arterial signals were either grade 1 (mixed signals) or grade 2 (entirely hyperintense signal) in 17 volunteers (94%) on all three types of imaging, and basilar intra-arterial signals were shown in grade 1 or grade 2 in 18 volunteers (100%) on sequential imaging, and in 17 volunteers (94%) on 100% interleaved and 200% interleaved imaging. Conversely, on all the three types of imaging with PP, vertebral and basilar intra-arterial signals showed no signal (grade 0). Intra-arterial signals were significantly suppressed with application of PP (Fig 5) ($P < .0001$).

DISCUSSION

This study revealed that interleaved SE T1-weighted imaging produced significantly higher GM-WM contrast than sequential SE T1-weighted imaging at 3 T. In addition, PP satisfactorily suppressed intra-arterial signals on SE T1-weighted imaging at 3 T.

We believe that cross-talk effect is one of the reasons why interleaved SE T1-weighted imaging offers better GM-WM contrast than sequential imaging at 3 T. Cross-talk effect is an important factor in the contrast on SE imaging, which can result in decreased signal and concomitant decreases in contrast (13,14). Cross-talk effect may be stronger in a higher magnetic field because recovery of the excited spin by cross-talk effect is prolonged due to longer T1-relaxation time. Interleaved acquisition acts to reduce cross-talk effect (13).

Magnetization transfer (MT) effect may be another reason why interleaved SE T1-weighted imaging offers better GM-WM contrast than sequential imaging at 3 T because sequential imaging has more radiofrequency pulses per TR interval than interleaved imaging. MT effect is an important factor in determining contrast (14,15), and is also a significant contributor to image contrast in multi-slice acquisition compared with single-slice acquisition (15,16), and this effect is stronger at higher fields (16–19). Furthermore, the present study showed that application of PP significantly reduced CNR_{GM-WM}. This could also be due to the MT effect caused by PP pulses. CNR_{GM-WM} reduction rate by the application of PP became less prominent with increased number of interleaved samplings. This could be explained that less number of imaging slices for each interleaved image acquisition leads to less MT effect caused by PP. We should be aware of prominent contrast reduction by the application of PP, especially in sequential and 100% interleaved sequences.

An advantage of SE T1-weighted imaging over GRE T1-weighted imaging is that intra-arterial signals are displayed as hypointense due to the flow-void effect, which enables differentiation between arterial flow and intra-arterial subacute clots. SE T1-weighted imaging at lower fields is thus well known as a useful sequence in diagnosing vascular lesions, such as arterial dissection (20) and intra-arterial thrombus (particularly subacute phase). SE T1-weighted imaging plays a complementary role in relation to MR angiography because MR angiography can misidentify high-intensity thrombus as flow in arteriovenous malformation, and methemoglobin in subacute thrombus can be hyperintense on source images of

Table 1
Vertebral and Basilar Intra-arterial Signal Grade in 18 Volunteers

	Sequential		100% Interleaved		200% Interleaved	
	Without PP	With PP	Without PP	With PP	Without PP	With PP
Vertebral artery						
Grade 0	1 (6)	18 (100)	1 (6)	18 (100)	1 (6)	18 (100)
Grade 1	2 (11)	0 (0)	4 (22)	0 (0)	4 (22)	0 (0)
Grade 2	15 (83)	0 (0)	13 (72)	0 (0)	13 (72)	0 (0)
P value	<.0001		<.0001		<.0001	
Basilar artery						
Grade 0	0 (0)	18 (100)	1 (6)	18 (100)	1 (6)	18 (100)
Grade 1	10 (56)	0 (0)	4 (22)	0 (0)	4 (22)	0 (0)
Grade 2	8 (44)	0 (0)	13 (72)	0 (0)	13 (72)	0 (0)
P value	<.0001		<.0001		<.0001	

Vertebral and basilar intra-arterial signal grading with or without presaturation pulse (PP). Grade 0, no signal; grade 1, mixed signals; grade 2, entirely hyperintense signal. Intra-arterial signals were significantly diminished by application of PP. Percentages are shown in parentheses.

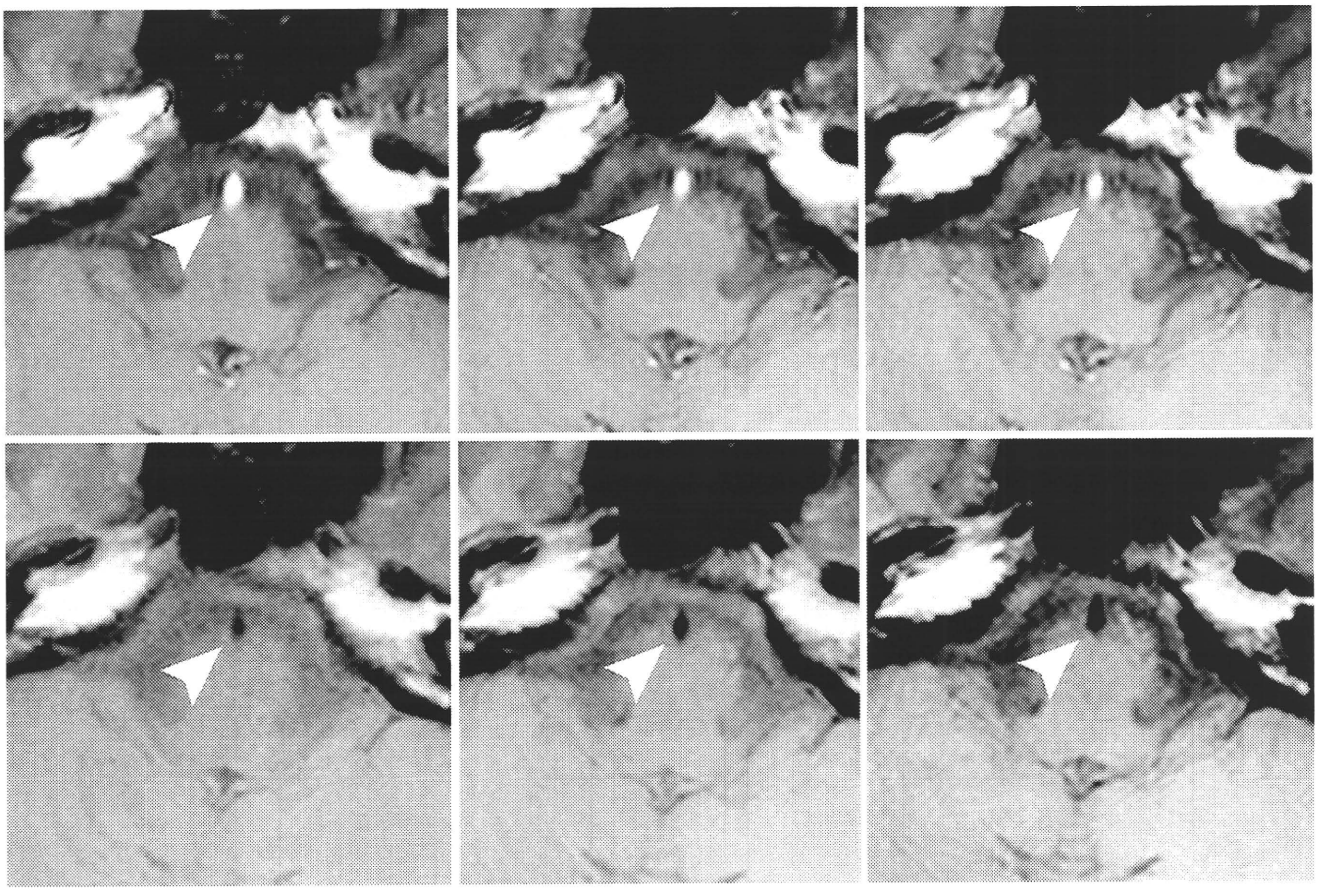

Figure 5. Spin-echo T1-weighted gapless multi-slice imaging at 3 T without presaturation pulse (PP) (*upper row*) and with PP (*lower row*) at the level of the pons. From left to right, sequential imaging, 100% interleaved imaging and 200% interleaved imaging are displayed. Basilar intra-arterial signals were sufficiently suppressed on imaging with PP (*lower row*).

MR angiography (9,21). At high fields such as 3 T, intra-arterial blood tends to be hyperintense because of increased paradoxical enhancement due to longer T1 relaxation time. In fact, in the present study, vertebral and basilar intra-arterial signals were displayed as hyperintense or mixed signals in ≥94% (17 of 18) of volunteers on all three types of imaging without PP. Consequently, SE T1-weighted imaging without PP may not be able to reveal some vascular diseases, such as

arterial dissection or intra-arterial thrombus. However, these vertebral and basilar intra-arterial signals were completely suppressed by PP, as shown in the current study. The present study demonstrated that PP effectively suppresses intra-arterial signal, even at 3 T.

Another advantage of SE sequence over GRE sequence in obtaining T1-weighted imaging is that SE imaging displays significantly fewer susceptibility artifacts than GRE imaging (8). Susceptibility artifacts degrade image quality at air/tissue interfaces, such as paranasal sinuses, temporal bone, and the pituitary gland (22,23). Furthermore, susceptibility artifacts are more enhanced at higher field strength (24,25). SE imaging would thus be more suitable than GRE imaging in evaluating lesions near air/tissue interfaces, such as pituitary adenoma at 3 T.

This study has several limitations. We have not optimized the imaging parameters, such as TR, TE, or slice thickness. Further studies are needed to optimize SE T1-weighted imaging parameters at 3 T for clinical use. Further studies are also needed to verify the usefulness of interleaved SE T1-weighted imaging with PP in diagnosing diseases, such as arterial dissection or pituitary adenoma, in which SE T1-weighted imaging has been reported as useful at lower fields. We did not analyze the contrast on T1-weighted fluid-attenuated inversion recovery (FLAIR) sequence. A previous study at 0.2T showed that T1-weighted FLAIR images had better CNR of GM-WM than SE T1-weighted images (26). However, another previous study at 1.5 T showed no significant difference in CNR of peripheral GM-WM between T1-weighted FLAIR and SE T1-weighted images (27). Contrast on T1-weighted FLAIR images may be affected by segmentation of the k-space due to multiple TEs and by increased MT effect attributable to multiple refocusing pulses. Future studies may be needed to quantitatively compare the contrast between GM and WM on SE T1-weighted sequence and T1-weighted FLAIR sequence at 3 T.

CONCLUSION

This study revealed that GM-WM contrast on SE T1-weighted imaging at 3 T can be improved by interleaved acquisition, and that PP satisfactorily suppresses intra-arterial signals. Interleaved SE T1-weighted imaging with PP could be clinically feasible at 3 T.

REFERENCES

1. Nobauer-Huhmann IM, Ba-Ssalamah A, Mlynarik V, et al. Magnetic resonance imaging contrast enhancement of brain tumors at 3 tesla versus 1.5 tesla. Invest Radiol 2002; 37:114–119.
2. Sasaki M, Inoue T, Tohyama K, et al. High-field MRI of the central nervous system: current approaches to clinical and microscopic imaging. Magn Reson Med Sci 2003; 2:133–139.
3. Scarabino T, Nemore F, Giannatempo GM, et al. 3.0 T magnetic resonance in neuroradiology. Eur J Radiol 2003; 48:154–164.
4. Ross JS. The high-field-strength curmudgeon. AJNR Am J Neuroradiol 2004; 25:168–169.
5. Kuhl CK, Traber F, Schild HH. Whole-body high-field-strength (3.0-T) MR imaging in clinical practice. Part I. Technical considerations and clinical applications. Radiology 2008; 246:675–696.
6. Schmitz BL, Gron G, Brausewetter F, et al. Enhancing gray-to-white matter contrast in 3 T T1 spin-echo brain scans by optimizing flip angle. AJNR Am J Neuroradiol 2005; 26:2000–2004.
7. Lu H, Nagae-Poetscher LM, Golay X, et al. Routine clinical brain MRI sequences for use at 3.0 Tesla. J Magn Reson Imaging 2005; 22:13–22.
8. Farahani K, Sinha U, Sinha S, et al. Effect of field strength on susceptibility artifacts in magnetic resonance imaging. Comput Med Imaging Graph 1990; 14:409–413.
9. Yousem DM, Balakrishnan J, Debrun GM, et al. Hyperintense thrombus on GRASS MR images: potential pitfall in flow evaluation. AJNR Am J Neuroradiol 1990; 11:51–58.
10. Fushimi Y, Miki Y, Urayama S, et al. Gray matter-white matter contrast on spin-echo T1-weighted images at 3 T and 1.5 T: a quantitative comparison study. Eur Radiol 2007; 17:2921–2925.
11. Felmlee JP, Ehman RL. Spatial presaturation: a method for suppressing flow artifacts and improving depiction of vascular anatomy in MR imaging. Radiology 1987; 164:559–564.
12. U.S. Department of Health and Human Services FDA, Center for Devices and Radiological Health Guidance for Industry and FDA Staff-Criteria for Significant Risk Investigations of Magnetic Resonance Diagnostic Devices. 2003. Available at:http://www.fda.gov/cdrh/ode/guidance/793.html. Accessed February 5, 2009.
13. Kneeland JB, Shimakawa A, Wehrli FW. Effect of intersection spacing on MR image contrast and study time. Radiology 1986; 158:819–822.
14. Majumdar S, Sostman HD, MacFall JR. Contrast and accuracy of relaxation time measurements in acquired and synthesized multislice magnetic resonance images. Invest Radiol 1989; 24:119–127.
15. Watanabe A, Boesch C, Obata T, et al. Effect of multislice acquisition on T1 and T2 measurements of articular cartilage at 3 T. J Magn Reson Imaging 2007; 26:109–117.
16. Chang Y, Bae SJ, Lee YJ, et al. Incidental magnetization transfer effects in multislice brain MRI at 3.0 T. J Magn Reson Imaging 2007; 25:862–865.
17. Duvvuri U, Roberts DA, Leigh JS, et al. Magnetization transfer imaging of the brain: A quantitative comparison of results obtained at 1.5 and 4.0 T. J Magn Reson Imaging 1999; 10:527–532.
18. Melhem ER, Jara H, Yucel EK. Multislice T1-weighted hybrid RARE in CNS imaging: assessment of magnetization transfer effects and artifacts. J Magn Reson Imaging 1996; 6:903–908.
19. Schmitz BL, Aschoff AJ, Hoffmann MH, et al. Advantages and pitfalls in 3 T MR brain imaging: a pictorial review. AJNR Am J Neuroradiol 2005; 26:2229–2237.
20. Mascalchi M, Bianchi MC, Mangiafico S, et al. MRI and MR angiography of vertebral artery dissection. Neuroradiology 1997; 39:329–340.
21. Hirabuki N, Fujita N, Hashimoto T, et al. Follow-up MRI in dural arteriovenous malformations involving the cavernous sinus: emphasis on detection of venous thrombosis. Neuroradiology 1992; 34:423–427.
22. Oehler MC, Schmalbrock P, Chakeres D, et al. Magnetic susceptibility artifacts on high-resolution MR of the temporal bone. AJNR Am J Neuroradiol 1995; 16:1135–1143.
23. Sakurai K, Fujita N, Harada K, et al. Magnetic susceptibility artifact in spin-echo MR imaging of the pituitary gland. AJNR Am J Neuroradiol 1992; 13:1301–1308.
24. Abduljalil AM, Robitaille PM. Macroscopic susceptibility in ultra high field MRI. J Comput Assist Tomogr 1999; 23:832–841.
25. Abduljalil AM, Kangarlu A, Yu Y, et al. Macroscopic susceptibility in ultra high field MRI. II: acquisition of spin echo images from the human head. J Comput Assist Tomogr 1999; 23:842–844.
26. Hori M, Okubo T, Uozumi K, et al. T1-weighted fluid-attenuated inversion recovery at low field strength: a viable alternative for T1-weighted intracranial imaging. AJNR Am J Neuroradiol 2003; 24:648–651.
27. Alibek S, Adamietz B, Cavallaro A, et al. Contrast-enhanced T1-weighted fluid-attenuated inversion-recovery BLADE magnetic resonance imaging of the brain: an alternative to spin-echo technique for detection of brain lesions in the unsedated pediatric patient? Acad Radiol 2008; 15:986–995.

Original Research

Visualization of the Lenticulostriate Artery With Flow-Sensitive Black-Blood Acquisition in Comparison With Time-of-Flight MR Angiography

Kimio Gotoh, MD,[1] Tomohisa Okada, MD, PhD,[1]* Yukio Miki, MD, PhD,[1] Masato Ikedo, BS,[2] Ayako Ninomiya, RT,[2] Toshikazu Kamae, MS,[1] and Kaori Togashi, MD, PhD[1]

Purpose: To evaluate the capability of flow-sensitive black blood (FSBB) acquisition to visualize the lenticulostriate artery (LSA) in comparison with time-of-flight (TOF) angiography.

Materials and Methods: Twenty-one healthy subjects (13 males and 8 females, 19–44 years old) were enrolled in this study after obtaining written informed consent. Magnetic resonance imaging (MRI) examinations were performed with FSBB and TOF to visualize the LSA using a 1.5T MRI unit. In FSBB acquisition a motion probing gradient of b = 4 sec/mm^2 was applied to dephase blood flow. Images were reconstructed into coronal sections and were evaluated in terms of number, length, and image quality at origins and distal areas of visualized LSA branches with a four-point scale.

Results: In all, 145 LSA branches were visualized with FSBB and 66 branches with TOF. There was no LSA visualized only with TOF. In all evaluated terms, FSBB was significantly better than TOF.

Conclusion: We could better visualize the LSA with FSBB than with TOF, both quantitatively and qualitatively. FSBB is a promising method, although it remains to be evaluated in clinical cases.

Key Words: lenticulostriate artery; flow-sensitive black blood; time-of-flight; MR angiography; diffusion
J. Magn. Reson. Imaging 2009;29:65–69.

THE LENTICULOSTRIATE ARTERY (LSA) originates mainly from the middle cerebral artery (MCA) and supplies blood to the basal ganglia and the internal capsule (1,2). Its occlusion results in lacunar infarct (3,4). In some of these patients, linear structures with abnormal density or signal were observed, consistent with occluded perforating arteries associated with the relevant lacunar infarct (5). In a prospective study of 93 patients of small subcortical infarcts, some relevance to MCA stenosis was observed but about 60% of cases were free of it (6). The LSA plays an important role for vascular disease at basal ganglia; however, its noninvasive visualization was limited.

Recently, susceptibility-weighted imaging (SWI) has been introduced as one of the ways of observing small vessels as black blood (7–9). In SWI, however, the flow rephasing is implemented and phase disturbance is observed mainly in the vein and its power for visualization of the artery is limited. On the other hand, signal from flowing blood can be attenuated by applying very weak motion probing gradients (dephase gradients), which mainly attenuates signal from moving blood in the artery and capillary, as well as in the vein (10), while the signal of the stationary component is almost intact, unlike diffusion-weighted images for stroke examination acquired with much larger motion probing gradients (MPGs). One such method proposed is flow-sensitive black blood (FSBB) acquisition (11,12).

Dilated LSA branches were visualized noninvasively with time-of-flight (TOF) MR angiography (MRA) in moya-moya patients (13). The TOF-MRA may visualize some branches of the LSA without dilatation, but invasive angiography is used for clinical evaluation (14) and the capability has not been much investigated.

From these considerations we hypothesized that the LSA would be better visualized with FSBB acquisition than with TOF-MRA and the purpose of this study was to examine and illustrate the advantage of using FSBB in comparison with TOF for visualization of the LSA.

MATERIALS AND METHODS

Subjects

Twenty-one healthy volunteers (13 males and 8 females; range 19–44 years old, mean 25 years old) with-

[1]Department of Diagnostic Radiology, Kyoto University Graduate School of Medicine, Kyoto, Japan.
[2]Toshiba Medical Systems Corp., Otawara-shi, Japan.
Contract grant sponsor: R&D of Molecular Imaging Equipment for Malignant Tumor Therapy Support, supported by New Energy and Industrial Technology Development Organization in Japan.
*Address reprint requests to: T.O., Department of Diagnostic Radiology, Kyoto University Graduate School of Medicine, 54 Shogoin Kawaharacho, Sakyoku, Kyoto, 606–8507, Japan. E-mail: tomokada@kuhp.kyoto-u.ac.jp
Received June 24, 2008; Accepted September 10, 2008.
DOI 10.1002/jmri.21626
Published online in Wiley InterScience (www.interscience.wiley.com).

out any known disease were enrolled in this study after obtaining written informed consent, based on the protocol approved by the Institutional Review Board.

Image Acquisition

The subjects were examined with both FSBB and TOF methods in order to visualize the LSA on a 1.5T MRI unit (EXCELART Vantage Powered by ATLAS, Toshiba Medical Systems, Otawara-shi, Japan). After obtaining localizing images of three orthogonal axis, T2-weighted fast spin echo images were acquired parallel to the AC (anterior commissure)-PC (posterior commissure) with the following parameters: TR/TE 4000/105 msec, flip angle 90/160°, acquisition matrix size 320 × 256, field of view (FOV) 220 × 180 mm, slice thickness 3 mm with 0.6 mm gap in 40 slices to cover the whole brain. In the same AC-PC slice orientation, TOF-MRA and FSBB images were scanned using the 3D gradient echo acquisition. The common imaging parameters were TR 29 msec, flip angle 20°, acquisition matrix size 256 × 224, FOV 205 × 179 mm in one axial 3D slab of 160 slices. The scan resolution was 0.8 × 0.8 × 0.8 mm, which was interpolated into 0.4 × 0.4 × 0.4 mm in order to increase apparent resolution and improve image quality after reformatting. The scan time was 6 minutes 35 seconds. In the TOF scan, TE was 6.8 msec and a magnetization transfer contrast pulse and flow rephasing were used. For the FSBB acquisition, TE was 20 msec and the motion probing gradient of b = 4 sec/mm^2 was evenly divided and applied to all three axes. At the initial stage we evaluated effect of MPG at different b values of 0, 1, 2, and 4 sec/mm^2 as a preliminary evaluation.

Image Analysis

The 3D image volume data was transferred to a commercially available workstation (AZE VirtualPlace Lexus, AZE, Tokyo, Japan) and the following processings and evaluations were conducted on the same workstation. After reorienting the 3D axial image volumes into coronal (perpendicular to the AC-PC line), each of five consecutive slices was projected by maximum intensity (ie, MIP of 2 mm thickness) for TOF and by minimum intensity (ie, MinIP of 2 mm thickness) for FSBB. By using these images, LSA branches were traced and measured for length on the workstation. On the reconstructed images, LSA branches longer than 5 mm were analyzed. When an artery branches within 5 mm from the MCA origin, each branch was counted and measured separately, because more than 70% of branches were found to originate from common trunks (1). When an artery branches at a more distal site, only the longest branch was counted and measured. Images were analyzed in terms of number, length, and quality of visualization for the visualized LSA branches using a four-point scale (0: not visualized, 1: poor, 2: good, and 3: excellent). The quality of visualization was evaluated separately at origins of the LSA and areas distal to them. The evaluation was performed for each and every visualized LSA branches in random order by two experienced radiologists in consensus, although we could not avoid evaluators noticing the acquisition method due to differences in appearance between FSBB and TOF images. The length of LSA branches was measured by another researcher. On the T2-weighted axial images, high-intensity spots were examined in the basal ganglia region above the anterior perforated substance and the number of the perivascular space was counted by two radiologists in consensus.

Statistical Analysis

The numbers of visualized branches per subject were compared between FSBB and TOF with a two-tailed paired *t*-test, separately for left and right hemispheres. The difference in numbers between left and right was also examined. Lengths of all visualized LSA branches were compared between FSBB and TOF with a two-tailed two-sample *t*-test. In the comparisons of scores for quality of visualization between FSBB and TOF, a Wilcoxon signed rank test was used. A *P*-value less than 0.05 was considered statistically significant. Statistical analyses were conducted using a commercially available software package (SPSS 16.0, SPSS, Chicago, IL).

RESULTS

Preliminary Evaluation

FSBB acquisitions were performed, with a certain range of b values (b = 0, 1, 2, and 4 s/mm^2; the last value was the maximum in the system). Representative images are shown in Fig. 1. Very few LSAs were visualized at b = 0 s/mm^2 and more of them were better depicted according to the increase of b values. Visualization was best at a b value of 4 s/mm^2, which was adopted for the current study.

Number and Length of Visualized LSAs

The average numbers and standard deviations of visualized LSAs per subject were 3.6 ± 1.2 and 1.5 ± 0.8 on the left, and 3.3 ± 1.0 and 1.7 ± 0.9 on the right for FSBB and TOF, respectively (Table 1). The differences between FSBB and TOF were significant ($P = 0.001$) on both sides; however, there was no significant difference between left and right for both FSBB and TOF ($P = 0.459$ and $P = 0.479$, respectively). The total number of branches visualized with FSBB was 145, and 66 (46%) were also visualized with TOF. There was no LSA that was visible only in TOF images. The average lengths of visualized LSA branches were 21.8 ± 7.1 mm and 18.6 ± 8.1 mm for FSBB and TOF, respectively (Table 1), which were statistically significantly different ($P = 0.008$). Some representative images are presented in Fig. 2 using thicker projected images (8 mm) than those used for analysis.

Quality of Visualization at Origins and Areas Distal to Them

Visualization scores are summarized in Table 2. At the origin of LSA branches, FSBB showed significantly better visualization of the LSA than TOF ($P = 0.003$). Also, at the areas distal to the origins, FSBB was better than TOF ($P = 0.001$). The results of the number, length, and

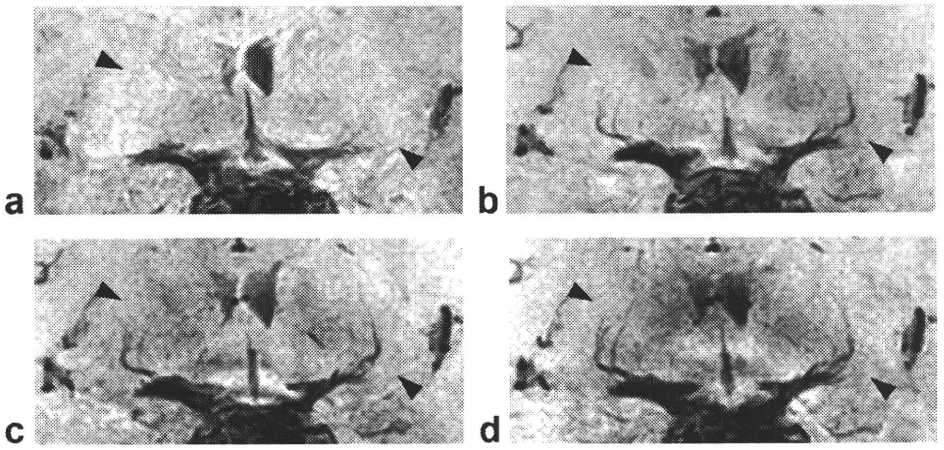

Figure 1. Differences in visualization of the lenticulostriate artery (LSA) dependent on the b values of motion probing gradient (MPG): b = 0, 1, 2, and 4 s/mm^2, as presented in images **(a–d)**, respectively. Better visualization of LSA is observed (see arrowheads) by increasing b values, whereas CSF signal is gradually decreased.

quality of visualization at distal areas for LSA branches visualized with FSBB and TOF are illustrated in Fig. 3.

Number of the Perivascular Space and Other Lesions on T2WI

No significantly abnormal finding was detected on T2WIs of all the subjects. The perivascular spaces were detected as tiny high intensity spots on axial T2WIs above the anterior perforated substance in some subjects, but the number was 7 in total and they were limited 1 to 2 slices above the slice with the anterior perforated substance.

DISCUSSION

Histological examination of the LSAs in the vascular casts of 48 middle cerebral arteries revealed that more than 90% of LSA branches originated from the first segment of the MCA (M1), and they ranged between 2 and 12 (mean 7.1) in number and from 80 μm to 1,400 μm in size (1). Another study reported that there were usually three branches in the middle group and one to nine in the lateral group (2). By using the FSBB method, we observed 3.6 and 3.3 branches on average on the left and right sides, respectively. These results conform to the aforementioned histological results. Although the whole branches of the LSA may not be visualized even with FSBB acquisition, length and quality of visualization were significantly better with FSBB scan than TOF-MRA, which requires rapid vascular inflow (15), and LSA branches were considered to be too small to fully visualize with the latter method. On the other hand, even slow flow can be dephased by a weak motion probing gradient and the FSBB acquisition was more sensitive in detecting small vessels with slow flow like the LSA. Although FSBB is suitable for visualizing small arteries, it might be used to evaluate a larger artery with turbulent flow. In patients with sickle cell disease, high-velocity flow secondary to anemia generates turbulence and it produces intimal injury and hyperplasia, resulting in infarction. But at the same time, this turbulence often causes pseudo-lesion on TOF-MRA (16). Although such cases are yet to be evaluated, intimal hyperplasia might show some signal on the FSBB image and it may help to avoid pseudo-lesions. In the FSBB image the perivascular space or cerebrospinal fluid (CSF) might possibly be detected as the same signal void. However, it should be noted that the number of the perivascular space detected on the T2WI was 7 in the whole subjects and they were limited within one or two slices above the anterior perforated substance. In aged subjects, the perivascular space would frequently be dilated, but CSF signal in the space is expected to be higher than LSA signal, which is void, as shown in Figs. 1 and 2. Calcification, small hemorrhage, and iron deposit would be visualized as signal void, but they would be identified as spotty, nodular, or even mass-like lesions and may not be recognized as "string-like" LSAs.

Table 1
Number and Length of Visualized LSA Branches

	Numbers		Length
	Left	Right	
FSBB	3.6 ± 1.2	3.3 ± 1.0	21.8 ± 7.1 (145)
TOF	1.5 ± 0.8	1.7 ± 0.9	18.6 ± 8.1 (66)
P value	$P = 0.001$	$P = 0.001$	$P = 0.008$

Numbers and length are presented in mean ± standard deviation, and total branch numbers are presented in parentheses.

Quality of visualization was evaluated at the origin of LSA branches, because understanding the microanatomy of the proximal middle cerebral artery (M1) and its branches is very important for aneurysm surgery. It may cause clipping or blood flow disturbance of LSA, resulting in cerebral infarction (17,18). Although aneurysm clipping is generally preceded by digital subtraction angiography (DSA), not all hospitals can use 3D-DSA. 3D and isotropic information of the FSBB image may complement bi-plane DSA. The average scores for the FSBB image were lower compared with those evaluated at distal areas. It was probably caused by the pulsatile motion of CSF, because gross motion causes signal reduction by MPG even at a b value of 4 s/mm^2. Hence, for better visualization at the origin a lower b value would be appropriate.

In the analysis axial slabs were reformatted into the coronal orientation and every five slices were projected and reconstructed as one slice of 2 mm thickness for minimum intensity in the FSBB images and for maximum intensity in the TOF images. Although thicker

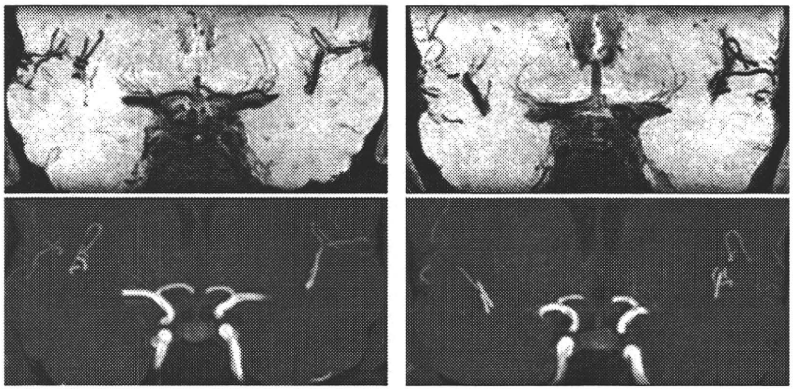

Figure 2. Representative images of LSA branches from two subjects (left and right columns). The upper row shows FSBB images and the lower shows TOF images. Better visualization is noted in images of FSBB than TOF.

slices allowed easier detection, measurement, and evaluation of the LSA, they might yield more errors, because LSA branches looked as if they were fusing each other when viewed on thick slices despite the observation that their anastomosis is very rare (19). On the other hand, when the slice was very thin tracing the continuity of an LSA branch was difficult and it caused some errors in measuring the entire length that was visualized. Hence, a minimum intensity projection of 2 mm slice thickness was adopted for better processing. For viewing purposes, however, thicker reformatting would be useful, as illustrated in Fig. 2 (8 mm thick).

In a series of cases with a small infarct in the territory of the LSAs more than 75% of the patients were either hypertensive or diabetic (20), both of which increase the risk of cerebrovascular disease, including in the areas of deep brain structures. For these patients, screening for abnormal findings of the LSA could be beneficial, as TOF-MRA has been made great contributions to completely noninvasive screening for abnormality of vasculatures of larger size. Cerebral hemorrhage in basal ganglia is also associated with LSA abnormalities, such as dissection, aneurysm, and abnormal dilatation. The microaneurysm of perforating arteries was suggested to be responsible for hypertension-induced cerebral hemorrhage (21). If some morphological changes in the LSA, such as hypovisualization, left–right asymmetry, and an aneurysm are visualized in asymptomatic patients of DM or hypertension, it may allow more rigorous therapeutic interventions to prevent symptomatic events, although further studies are required to clarify a causality linkage between FSBB findings and future morbidity. The noninvasive nature of FSBB acquisition would also enable regular follow-up observations. The FSBB acquisition is a noninvasive modality and may play an important role in assessing the LSA.

There are some limitations in this study. First, almost all the subjects were younger than 40 years old and the range of subject age was limited because this study intended to evaluate the feasibility of FSBB acquisition to visualize the LSA. Further studies on patients of lacunae, DM, hypertension, and others are yet to be made. Second is the absence of a reference standard. Conventional angiography may better visualize the LSA; however, angiographic images of healthy volunteers were not obtainable because the procedure is invasive and has some risk of complications. Lastly, FSBB is better at visualizing small and slow-flow arteries. For larger arteries, TOF visualizes better and is suitable for multidirectional MIP observation. Therefore, FSBB should be used complementary to TOF.

Table 2
Visualization Scores for LSA Branches

	FSBB	TOF
Origin		
3	43	16
2	66	17
1	34	25
0	2	8
Total	145[a]	66
Distal area		
3	67	7
2	64	28
1	14	31
Total	145[b]	66

[a]$P = 0.003$, [b]$P = 0.001$.

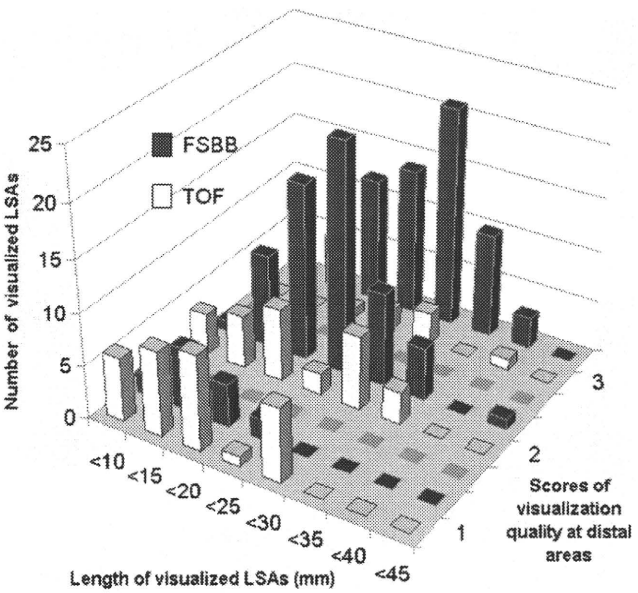

Figure 3. A histogram presentation of numbers, length, and quality scores at distal areas for 145 and 66 LSA branches visualized by FSBB and TOF, respectively. It is illustrated that FSBB visualized longer at higher quality than TOF.